


RESEARCH ARTICLE

Open Access



# Differentiating brain metastasis from glioblastoma by time-dependent diffusion MRI

Kiyohisa Kamimura<sup>1\*</sup> , Yoshiki Kamimura<sup>2</sup>, Tsubasa Nakano<sup>2</sup>, Tomohito Hasegawa<sup>2</sup>, Masanori Nakajo<sup>2</sup>, Chihiro Yamada<sup>2</sup>, Kentaro Akune<sup>2</sup>, Fumitaka Ejima<sup>2</sup>, Takuro Ayukawa<sup>2</sup>, Soichiro Ito<sup>2</sup>, Hiroaki Nagano<sup>2</sup>, Koji Takumi<sup>2</sup>, Masatoyo Nakajo<sup>2</sup>, Hiroyuki Uchida<sup>3</sup>, Kazuhiro Tabata<sup>4</sup>, Takashi Iwanaga<sup>5</sup>, Hiroshi Imai<sup>6</sup>, Thorsten Feiweier<sup>7</sup> and Takashi Yoshiura<sup>1,2</sup>

## Abstract

**Background** This study was designed to investigate the use of time-dependent diffusion magnetic resonance imaging (MRI) parameters in distinguishing between glioblastomas and brain metastases.

**Methods** A retrospective study was conducted involving 65 patients with glioblastomas and 27 patients with metastases using a diffusion-weighted imaging sequence with oscillating gradient spin-echo (OGSE, 50 Hz) and a conventional pulsed gradient spin-echo (PGSE, 0 Hz) sequence. In addition to apparent diffusion coefficient (ADC) maps from two sequences ( $ADC_{50\text{Hz}}$  and  $ADC_{0\text{Hz}}$ ), we generated maps of the ADC change (cADC):  $ADC_{50\text{Hz}} - ADC_{0\text{Hz}}$  and the relative ADC change (rcADC):  $(ADC_{50\text{Hz}} - ADC_{0\text{Hz}}) / ADC_{0\text{Hz}} \times 100$  (%).

**Results** The mean and the fifth and 95th percentile values of each parameter in enhancing and peritumoral regions were compared between glioblastomas and metastases. The area under the receiver operating characteristic curve (AUC) values of the best discriminating indices were compared. In enhancing regions, none of the indices of  $ADC_{0\text{Hz}}$  and  $ADC_{50\text{Hz}}$  showed significant differences between metastases and glioblastomas. The mean cADC and rcADC values of metastases were significantly higher than those of glioblastomas ( $0.24 \pm 0.12 \times 10^{-3} \text{mm}^2/\text{s}$  vs.  $0.14 \pm 0.03 \times 10^{-3} \text{mm}^2/\text{s}$  and  $23.3 \pm 9.4\%$  vs.  $14.0 \pm 4.7\%$ ; all  $p < 0.01$ ). In peritumoral regions, no significant difference in all ADC indices was observed between metastases and glioblastomas. The AUC values for the mean cADC (0.877) and rcADC (0.819) values in enhancing regions were significantly higher than those for  $ADC_{0\text{Hz}}^{5\text{th}}$  (0.595; all  $p < 0.001$ ).

**Conclusions** The time-dependent diffusion MRI parameters may be useful for differentiating brain metastases from glioblastomas.

**Keywords** Diffusion, Glioblastoma, Magnetic resonance imaging, Neoplasm metastasis

\*Correspondence:

Kiyohisa Kamimura

kiyohisa@m2.kufm.kagoshima-u.ac.jp

Full list of author information is available at the end of the article



© The Author(s) 2023. **Open Access** This article is licensed under a Creative Commons Attribution 4.0 International License, which permits use, sharing, adaptation, distribution and reproduction in any medium or format, as long as you give appropriate credit to the original author(s) and the source, provide a link to the Creative Commons licence, and indicate if changes were made. The images or other third party material in this article are included in the article's Creative Commons licence, unless indicated otherwise in a credit line to the material. If material is not included in the article's Creative Commons licence and your intended use is not permitted by statutory regulation or exceeds the permitted use, you will need to obtain permission directly from the copyright holder. To view a copy of this licence, visit <http://creativecommons.org/licenses/by/4.0/>. The Creative Commons Public Domain Dedication waiver (<http://creativecommons.org/publicdomain/zero/1.0/>) applies to the data made available in this article, unless otherwise stated in a credit line to the data.

## Background

Glioblastomas and brain metastases are the most common intra-axial brain tumors in adults. Since these two tumor types are substantially different with respect to clinical workup and therapeutic strategies [1], their pre-treatment differentiation is essential. Magnetic resonance imaging (MRI) is the modality of choice for the preoperative imaging assessment of brain tumors. However, differentiating brain metastases from glioblastomas based on conventional MRI may be difficult, as their findings are sometimes similar [2]. Diffusion-weighted imaging (DWI) reflects the Brownian motion of water molecules. DWI and quantitative measurement of the apparent diffusion coefficient (ADC) add valuable information regarding microstructures of tumor tissues to the conventional MRI findings. A weak to moderate inverse relationship was observed between ADC values and tumor cellularity [3–5]. Studies have shown that ADC values can help differentiate between certain types of brain tumors: malignant and benign meningiomas; high- and low-grade gliomas; and glioblastomas and primary central nervous system lymphomas [6–8]. However, the usefulness of the ADC values in differentiating brain metastases from glioblastomas remains controversial [9–12].

Diffusion time is an essential parameter of a DWI sequence that determines the duration over which water diffusion is assessed [13]. The ADC value matches the true diffusion coefficient only when diffusion is free (Gaussian), and this diffusion coefficient does not depend on the b-values or the diffusion time. However, when diffusion in tissues is not Gaussian, it depends on the interactions of molecules with spatial barriers, such as fibers and cell membranes (restricted diffusion). In the presence of restricted diffusion, the ADC values increase with decreasing diffusion time [14–17]. In conventional DWI based on pulsed gradient spin-echo (PGSE), high b-value is used to probe restricted diffusion, leading to a long diffusion time due to the limited maximum achievable gradient strength in clinical MRI systems [18, 19]. Recently, the oscillating gradient spin-echo (OGSE) method has become available on clinical MRI scanner [14]. This method can shorten the diffusion time by substituting the long diffusion sensitizing gradients used in PGSE methods with rapid oscillation gradients. DWI with the OGSE method enables to shorten the diffusion times and thus allows the exploration of the ADC diffusion time dependencies at the short diffusion time regime, which are inaccessible using the PGSE method alone. Time-dependent diffusion MRI is considered to provide more detailed information regarding tissue microstructure and has currently been tested in clinical settings to evaluate normal brains [14, 20], intracranial epidermoid cysts [21], head and neck tumors [22], and brain tumors [23]. It is

conceivable that brain metastases originating from outside the central nervous system substantially differ from glioblastomas in terms of microstructure. In particular, epithelial tumors in the body are characterized by cell–cell adhesion that can narrow the extracellular space. This microstructural feature may be associated with a higher volume fraction of the intracellular space, where water molecular diffusion is restricted by the cell membrane and a clear diffusion time dependence of water diffusion is present [24]. We hypothesized that time-dependent diffusion MRI can detect such microstructural feature of brain metastasis, providing a valuable clue to the differentiation from glioblastoma. Thus, our purpose was to investigate the usefulness of the time-dependent diffusion MRI parameters obtained using the OGSE and PGSE methods in differentiating brain metastases from glioblastomas.

## Materials and methods

### Patients

Our Institutional Review Board approved this retrospective study (approval no. 220126) and waived the need for written informed consent. The inclusion criteria were consecutive patients with pathologically proven glioblastoma or brain metastasis who underwent MRI including OGSE and PGSE sequences as a part of routine pretreatment assessments between January 2019 and September 2022 at our institution. All glioblastomas were diagnosed based on an integrated diagnosis combining histology and a glioma-tailored next-generation sequencing panel developed in our institution [25], and fulfilled the World Health Organization classification of 2021 [26]. The exclusion criteria were (a) lack of preoperative MRI, including DWI with both OGSE and PGSE sequences; (b) poor image quality; (c) masses smaller than 1 cm; (d) previous surgical resection or irradiation; or (e) lack of contrast-enhancing lesions.

In patients with multiple lesions, the largest mass was examined by MRI.

In this study, 175 consecutive patients (121 with glioblastomas and 54 with brain metastases) were considered. Among them, 83 were excluded owing to the absence of preoperative MRI including both OGSE and PGSE DWI scans (49 with glioblastomas and 25 with brain metastases), masses smaller than 1 cm (two with brain metastases), poor image quality caused by artifacts in the DWIs (three with glioblastomas), previous surgical resection or irradiation (two with glioblastomas), or lack of contrast-enhancing lesions (two with glioblastomas). Thus, 92 patients (56 men and 36 women; age range, 15–91 years; mean age,  $69 \pm 12$  years) met the inclusion criteria. Sixty-five patients with isocitrate dehydrogenase-wildtype

glioblastomas (37 men and 28 women; age range 15–91 years; mean age,  $69 \pm 13$  years) and 27 with brain metastases (19 men and eight women; age range 47–80 years; mean age,  $68 \pm 10$  years; 15 from lung cancer, four from breast cancer, three from colon cancer, two from gastric cancer, one from bladder cancer, one from submandibular cancer, and one from spindle cell sarcoma) were finally analyzed (Fig. 1). Eight patients had multiple brain metastases. No patient was treated for brain tumor before MRI. Histopathological confirmation was obtained based on total or partial surgical resection in all patients. Table 1 shows the characteristics of the patients. Sixty-five patients were diagnosed with glioblastomas, and 27 were diagnosed with brain metastases. No significant differences in age and sex were observed between patients with glioblastomas and those with brain metastases.

**MRI acquisition**

All patients were scanned on a 3 T MR scanner (MAGNETOM Prisma; Siemens Healthcare; maximum gradient amplitude=80 mT/m, maximum slew rate=200 T/m/s for each gradient axis with a 20-channel head radiofrequency receive coil. DWI was performed with research sequences for the OGSE DWI using b-values of 0 s/mm<sup>2</sup> (number of excitation: 1) and 1,500 s/mm<sup>2</sup> (number of excitations: 4) and three diffusion encoding directions. OGSE diffusion encoding used trapezoid-sine waveforms [27] with an effective diffusion time ( $\Delta_{\text{eff}}$ ) of 7.1 ms (frequency=50 Hz; diffusion gradient pulse duration [ $\delta$ ]=8.5 ms). The  $\Delta_{\text{eff}}$  for the PGSE encoding was 44.5 ms (frequency=0 Hz; diffusion gradient separation [ $\Delta$ ]=59.8 ms;  $\delta$ =46.1 ms). The two sequences shared the following parameters: repetition time (TR), 4,600 ms; echo time (TE), 120 ms; field of view (FOV), 230×230

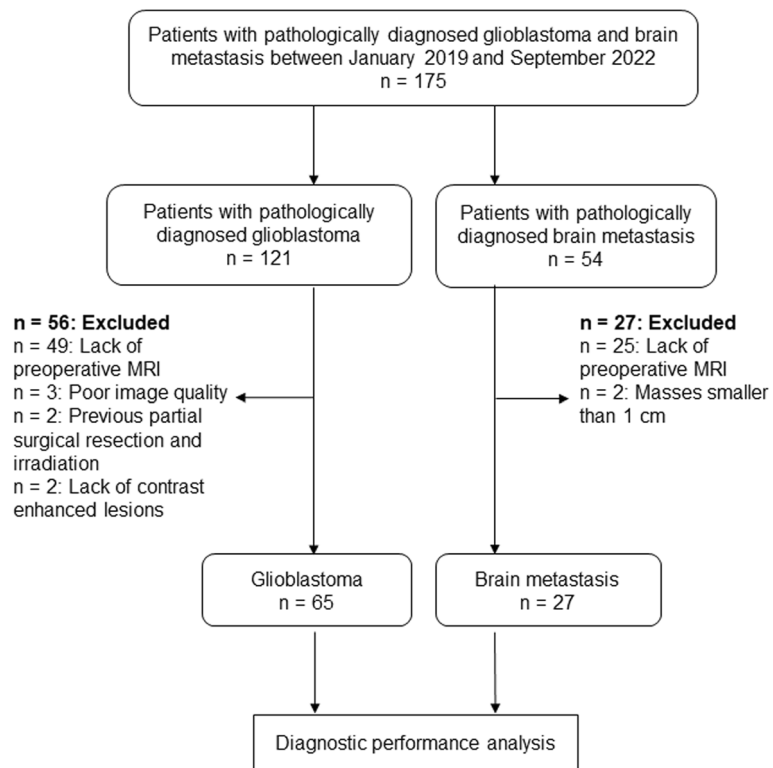


**Fig. 1** The study chart shows the inclusion and exclusion criteria and pathways for eligible patients in this study

**Table 1** Characteristics of the patients

Patients' characteristics	Total (n = 92)	Glioblastoma (n = 65)	Brain metastasis (n = 27)	p Value
Age (y)	69 ± 12	69 ± 13	68 ± 10	0.49 <sup>a</sup>
No. of men	56 (60.9%)	37 (56.9%)	19 (70.4%)	0.23 <sup>b</sup>

Statistical tests used: <sup>a</sup>Mann–Whitney U test, <sup>b</sup>chi-square test

mm<sup>2</sup>; matrix size, 72×72; number of slices, 24; and slice thickness, 5 mm. The acquisition times for PGSE DWI and OGSE DWI were 1 min and 13 s, and 1 min and 19 s, respectively. The pulse sequence diagrams for OGSE and PGSE are shown in Fig. 2.

Precontrast 2D fluid-attenuated inversion recovery (FLAIR) images were acquired using the following parameters: TR, 9,000 ms; TE, 121 ms; TI, 2,530 ms; number of excitations, 1; matrix, 307×384 (reconstructed to 768×768); number of slices, 24; slice thickness, 5 mm; interslice gap, 1 mm; FOV, 230×230 mm<sup>2</sup>; and scan time, 2 min and 6 s, and postcontrast 2D T1-weighted spin-echo images were also acquired using the following parameters: TR, 520 ms; TE, 12 ms; number of excitations, 1; matrix, 269×384 (reconstructed to 768×768); number of slices, 24; slice thickness, 5 mm; interslice gap, 1 mm; FOV, 230×230 mm<sup>2</sup>; and scan time, 2 min and 26 s. Then, these images were used for anatomical reference during the delineation of the region of interests (ROIs). In addition, our routine imaging for

the central nervous system region included the following precontrast sequences (Table 2): 2D T1-weighted spin-echo imaging, 2D T2-weighted turbo spin-echo imaging, and 3D susceptibility-weighted imaging. These sequences were not actively used in this study, although precontrast T1-weighted images were used to confirm contrast enhancement.

#### Delineation of the ROI

Two independent radiologists (T.H. and Y.K., with 7 and 3 years of radiological experience, respectively), who were blinded to the patients' clinical and pathological information, performed the ROI analysis using a commercially available software (Vitrea; Canon Medical Systems Corporation). ROIs were placed manually on a postcontrast T1-weighted image with the largest tumor diameter, including enhancing region and avoiding necrosis and fluid, such as nonenhancing regions in the tumor, and on the corresponding FLAIR image, including nonenhancing peritumoral regions with a FLAIR high

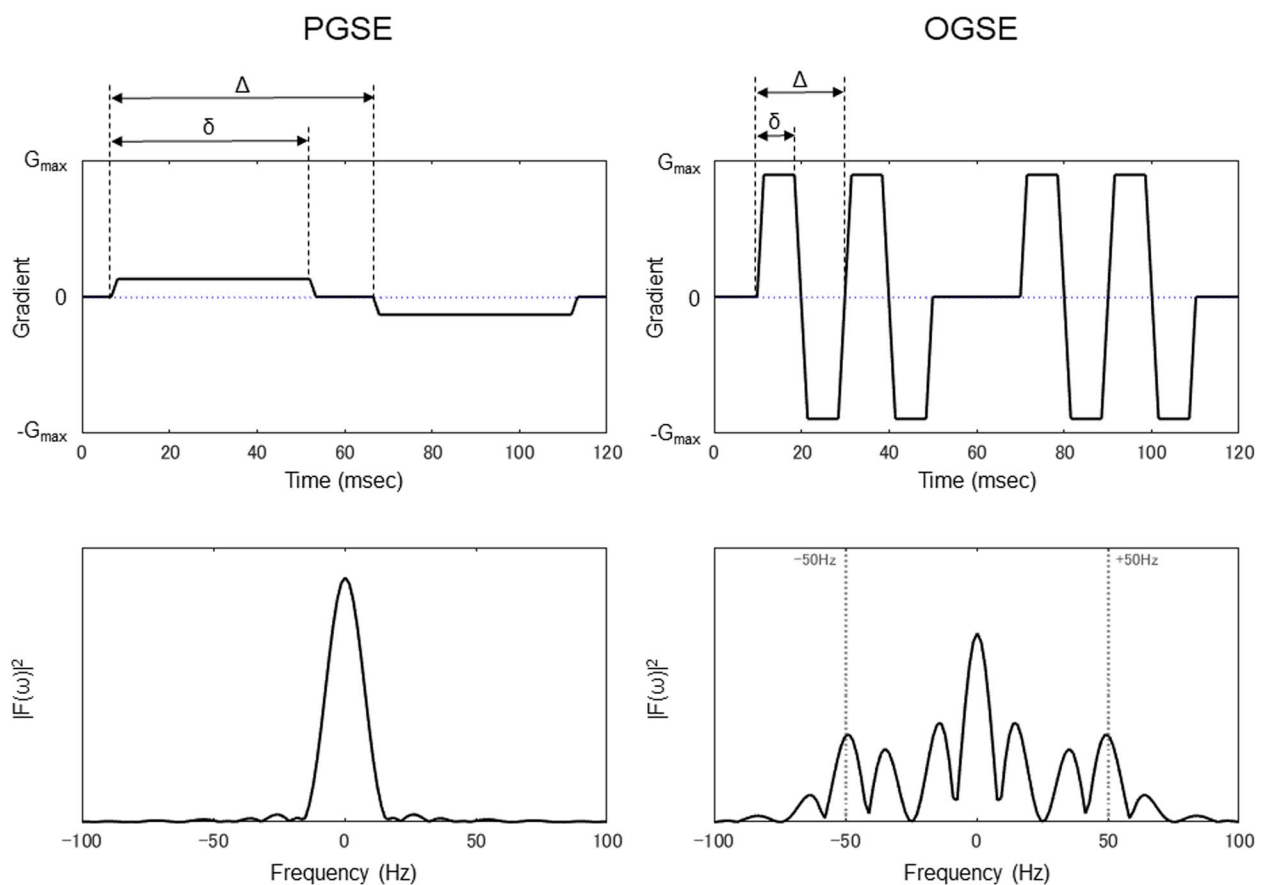


**Fig. 2** Schematic representation of the diffusion gradient waveforms, (top line) and their corresponding diffusion encoding spectra,  $|F(\omega)|^2$ , (bottom line) for pulsed gradient spin-echo (PGSE) (left) and oscillating gradient spin-echo (OGSE) (right). A 180° RF pulse is applied to the center of the gradient pair; therefore, the second gradient waveform acts as the opposite polarity.  $\Delta_{eff} = \Delta - \delta/3$ .  $\Delta_{eff}$ , effective diffusion time;  $\Delta$ , diffusion gradient separation;  $\delta$ , diffusion gradient pulse duration

**Table 2** Imaging parameters of pre and postcontrast conventional MRI sequences

	Precontrast 2D T1-weighted imaging	2D T2-weighted imaging	2D fluid-attenuated inversion recovery imaging	3D susceptibility-weighted imaging	Postcontrast 2D T1-weighted imaging
Sequence	2D SE	2D TSE	2D IR-TSE	3D FLASH	2D SE
TR (ms)	520	4000	9000	28	520
TE (ms)	12	91	121	20	12
TI (ms)	N/A	N/A	2530	N/A	N/A
FA (degree)	70/180	150	120	15	70/180
Bandwidth (Hz/pixel)	181	199	130	120	181
Number of excitations	1	1	1	1	1
Turbo factor	N/A	9	25	N/A	N/A
Acceleration factor	N/A	2	2	2	N/A
FOV (mm)	230	230	230	230	230
Matrix	269 × 384	380 × 448	307 × 384	240 × 320	269 × 384
Thickness (mm)	5	5	5	2.5	5
Intersection gap (mm)	1	1	1	N/A	1
Acquisition time (s)	148	80	126	174	148

signal intensity. The ROI size of the enhancing and the nonenhancing peritumoral regions was  $653 \pm 488 \text{ mm}^2$  (range, 113–2,383  $\text{mm}^2$ ) and  $622 \pm 607 \text{ mm}^2$  (28–2,817  $\text{mm}^2$ ), respectively, for glioblastomas, and  $437 \pm 290 \text{ mm}^2$  (252–894  $\text{mm}^2$ ) and  $925 \pm 773 \text{ mm}^2$  (59–3,495  $\text{mm}^2$ ), respectively, for brain metastases.

### Processing

ADC values were calculated, as follows:

$$\text{ADC} = \ln(S_0/S_1)/(b_1 - b_0), \quad (1)$$

where  $S_0$  and  $S_1$  are the signal intensities measured from DWI obtained using lower ( $b_0$ ) and higher ( $b_1$ ) b-values.

Researchers have evaluated the diffusion time dependence of ADC by calculating the change in the ADC between the OGSE and PGSE sequences and its ratio to the ADC derived from PGSE [22, 23]. We used both the ADC change (cADC) and the relative ADC change (rcADC) between OGSE and PGSE. cADC and rcADC maps were generated using the pixel-by-pixel calculation method, using the following formulas:

$$\text{cADC} = \text{ADC}_{50\text{Hz}} - \text{ADC}_{0\text{Hz}}, \quad (2)$$

$$\text{rcADC} = (\text{ADC}_{50\text{Hz}} - \text{ADC}_{0\text{Hz}})/\text{ADC}_{0\text{Hz}} \times 100(\%), \quad (3)$$

where  $\text{ADC}_{50\text{Hz}}$  and  $\text{ADC}_{0\text{Hz}}$  are the ADC values obtained using a DWI sequence with OGSE (50 Hz) and a conventional PGSE (0 Hz) sequence, respectively.

### ROI-based measurement

The ADC maps were coregistered with the postcontrast T1-weighted images using the rigid body registration on Vitrea. The ROIs of the enhancing region drawn on the postcontrast T1-weighted images and the ROIs of the peritumoral region drawn on the FLAIR images were duplicated on each ADC map and cADC and rcADC maps. Using the ROIs, the mean  $\text{ADC}_{0\text{Hz}}$  ( $\text{ADC}_{0\text{Hz}}^{\text{mean}}$ ),  $\text{ADC}_{50\text{Hz}}$  ( $\text{ADC}_{50\text{Hz}}^{\text{mean}}$ ), cADC ( $\text{cADC}^{\text{mean}}$ ), and rcADC ( $\text{rcADC}^{\text{mean}}$ ) were calculated for the entire ROI. In addition, the fifth and 95th percentiles of the  $\text{ADC}_{0\text{Hz}}$  ( $\text{ADC}_{0\text{Hz}}^{5\text{th}}$  and  $\text{ADC}_{0\text{Hz}}^{95\text{th}}$ ),  $\text{ADC}_{50\text{Hz}}$  ( $\text{ADC}_{50\text{Hz}}^{5\text{th}}$  and  $\text{ADC}_{50\text{Hz}}^{95\text{th}}$ ), cADC ( $\text{cADC}^{5\text{th}}$  and  $\text{cADC}^{95\text{th}}$ ), and rcADC ( $\text{rcADC}^{5\text{th}}$  and  $\text{rcADC}^{95\text{th}}$ ) were calculated, with these being considered to be representative of the lowest and highest robust values, respectively [28].

### Statistical analysis

The D'Agostino–Pearson normality test was used to verify the normality of the data obtained. The mean age was compared between those who had brain metastases and those who had glioblastoma using the Mann–Whitney  $U$  test, and the gender distribution was compared using the chi-square test. The interobserver agreement on parametric measures between the two observers was analyzed by computing the intraclass correlation coefficient (ICC). ICCs over 0.74 indicate excellent agreement [29]. Measurements taken by both observers for each patient



were averaged for more in-depth analysis. The paired- $t$  test was used for comparison of the ADC values with different diffusion times. The unpaired  $t$  test or Mann–Whitney  $U$  test was used for the comparison of the mean and the fifth and 95th percentiles of  $ADC_{0Hz}$ ,  $ADC_{50Hz}$ , cADC, and rcADC values. The area under the receiver operating characteristic curve (AUC) of each parameter was calculated. Sensitivity and specificity were obtained using a threshold criterion to maximize the Youden index. Differences in diagnostic performance were investigated with AUCs. In the enhancing regions, the most effective indices were determined for each  $ADC_{0Hz}$ ,  $ADC_{50Hz}$ , cADC, and rcADC. The AUCs of the most effective indices were compared using DeLong's test. Bonferroni correction was done to accommodate multiple comparisons. Statistical analyses were carried out using commercially available software packages (MedCalc, version 15.10.0; MedCalc statistical software).  $P$  values smaller than 0.05 were used to indicate statistical significance.

## Results

The representative diffusion parametric maps of glioblastoma and brain metastasis are shown in Figs. 3 and 4.

### Interobserver agreement

The ICCs and 95% confidence intervals for each parameter are shown in Table 3. All parameters showed an excellent agreement.

### Diffusion indices of brain metastases and glioblastomas

The  $ADC_{0Hz}^{mean}$ ,  $ADC_{0Hz}^{5th}$ ,  $ADC_{0Hz}^{95th}$ ,  $ADC_{50Hz}^{mean}$ ,  $ADC_{50Hz}^{5th}$ , and  $ADC_{50Hz}^{95th}$  values of the enhancing regions for glioblastomas and brain metastases are tabulated in Fig. 5a–c. For both tumors, all three indices for  $ADC_{50Hz}$  were significantly higher than those of  $ADC_{0Hz}$  (all  $p < 0.01$ , respectively) (Fig. 5a–c). No significant difference was observed between brain metastases and glioblastomas in any of the three indices of  $ADC_{0Hz}$  and  $ADC_{50Hz}$  (Fig. 5a–c). The  $cADC^{mean}$  ( $p < 0.01$ ),  $cADC^{5th}$  ( $p < 0.05$ ),  $cADC^{95th}$  ( $p < 0.01$ ),  $rcADC^{mean}$  ( $p < 0.01$ ),

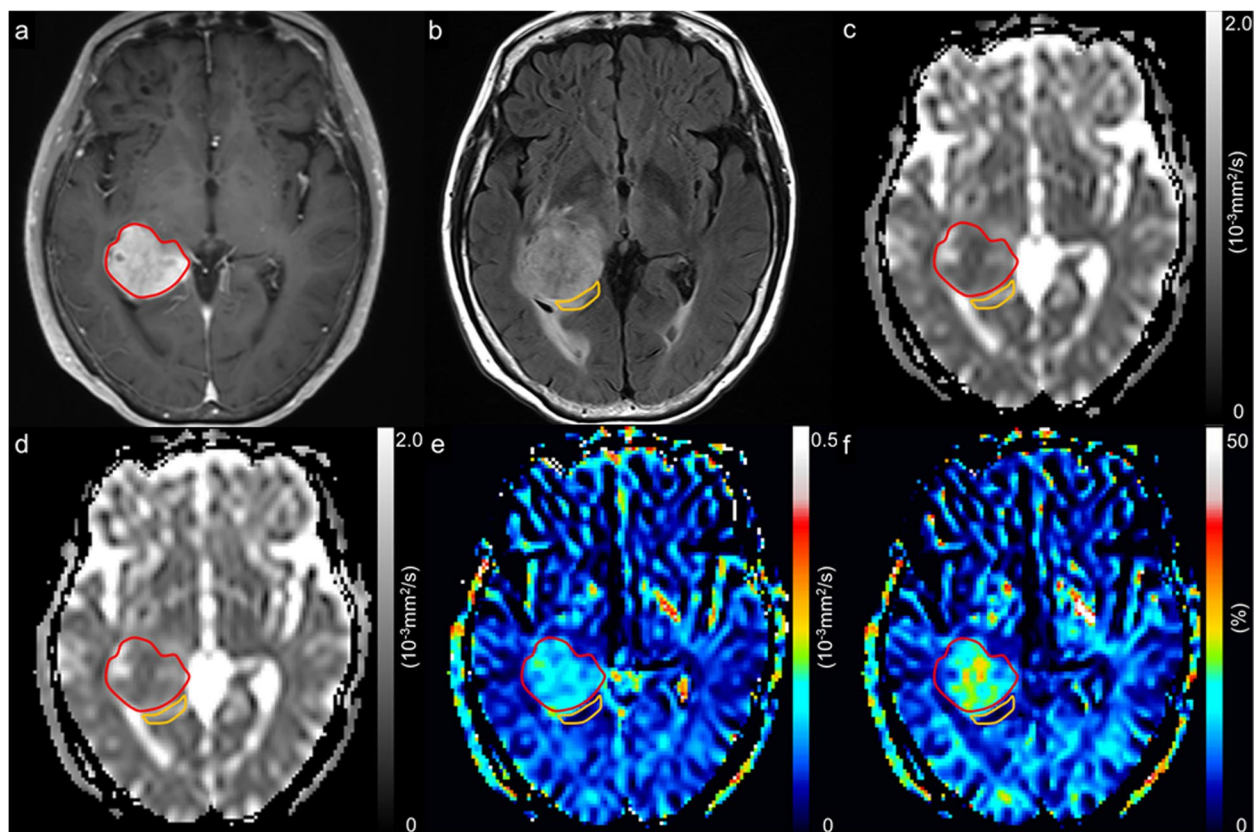


**Fig. 3** A 74-year-old woman with glioblastoma, isocitrate dehydrogenase-wildtype, grade 4. A contrast-enhanced T1-weighted image with a region of interest of the enhancing region (red line) (a), a FLAIR image with a region of interest of peritumoral region (orange line) (b), an apparent diffusion coefficient (ADC) map derived from pulsed gradient spin-echo (PGSE) DWI at an effective diffusion time ( $\Delta_{eff}$ ) of 44.5 ms (c), an ADC map derived from oscillating gradient spin-echo (OGSE) DWI at an  $\Delta_{eff}$  of 7.1 ms (d), and maps of ADC change between PGSE DWI and OGSE DWI (cADC) (e) and relative ADC change between PGSE DWI and OGSE DWI (rcADC) (f). The ADC values in the tumor appear higher at short  $\Delta_{eff}$  values than at long  $\Delta_{eff}$  setting. Small changes in cADC and rcADC are noted between the OGSE and PGSE sequences in the tumor

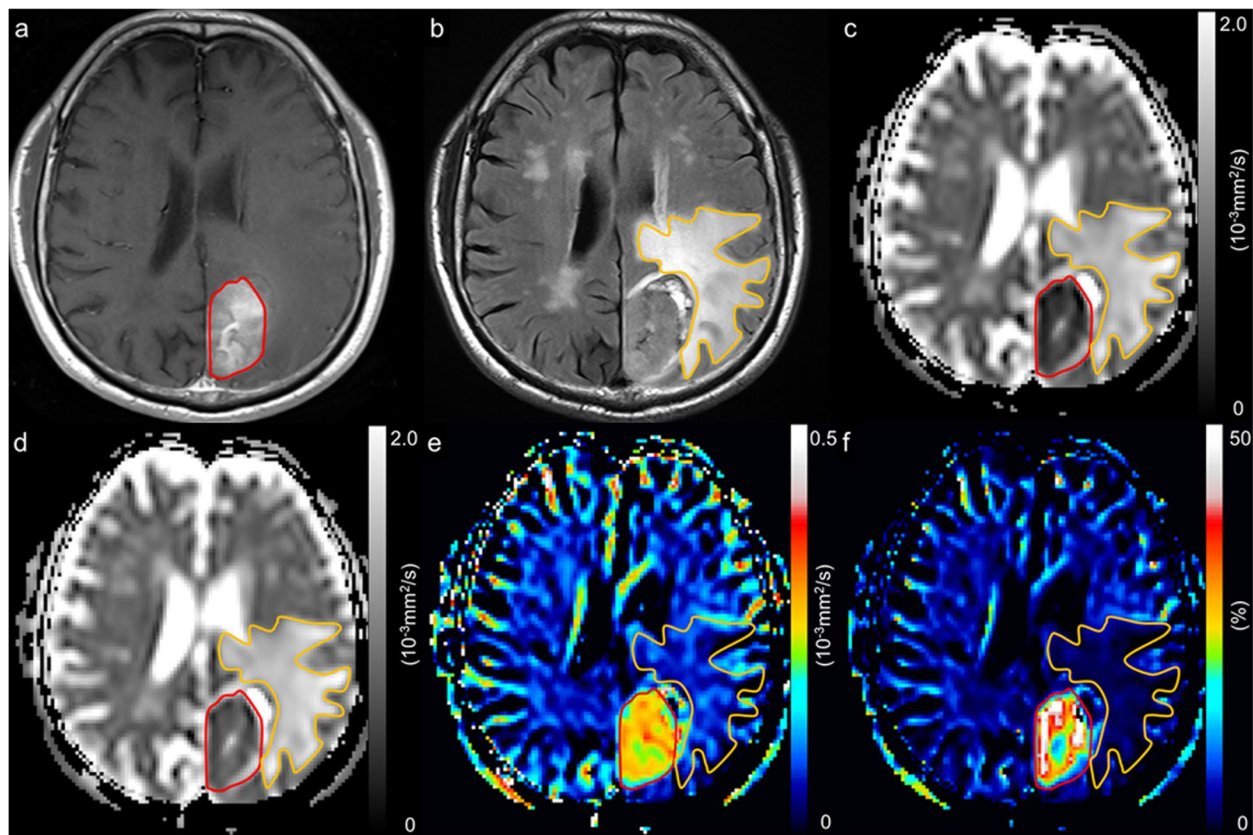


**Fig. 4** A 69-year-old man with a brain metastasis from colon cancer. A contrast-enhanced T1-weighted image with a region of interest of the enhancing region (red line) (a), a FLAIR image with a region of interest of peritumoral region (orange line) (b), an apparent diffusion coefficient (ADC) map derived from pulsed gradient spin-echo (PGSE) DWI at an effective diffusion time ( $\Delta_{\text{eff}}$ ) of 44.5 ms (c), an ADC map derived from oscillating gradient spin-echo (OGSE) DWI at an  $\Delta_{\text{eff}}$  of 7.1 ms (d), and maps of ADC change between PGSE DWI and OGSE DWI (cADC) (e) and relative ADC change between PGSE DWI and OGSE DWI (rcADC) (f). The ADC values in the tumor appear higher at short  $\Delta_{\text{eff}}$  values than at long  $\Delta_{\text{eff}}$  setting. Large changes in cADC and rcADC are noted between the OGSE and PGSE sequences in the tumor

**Table 3** The intraclass correlation coefficients and 95% confidence intervals for  $\text{ADC}_{0\text{Hz}}^{\text{mean}}$ ,  $\text{ADC}_{0\text{Hz}}^{5\text{th}}$ ,  $\text{ADC}_{0\text{Hz}}^{95\text{th}}$ ,  $\text{ADC}_{50\text{Hz}}^{\text{mean}}$ ,  $\text{ADC}_{50\text{Hz}}^{5\text{th}}$ ,  $\text{ADC}_{50\text{Hz}}^{95\text{th}}$ , cADC<sup>mean</sup>, cADC<sup>5th</sup>, cADC<sup>95th</sup>, rcADC<sup>mean</sup>, rcADC<sup>5th</sup>, and rcADC<sup>95th</sup> of the enhancing and peritumoral regions

Parameters	Intraclass correlation coefficients (95% confidence intervals)	
	Enhancing region	Peritumoral region
$\text{ADC}_{0\text{Hz}}^{\text{mean}}$	0.961 (0.943–0.974)	0.993 (0.989–0.995)
$\text{ADC}_{0\text{Hz}}^{5\text{th}}$	0.905 (0.860–0.936)	0.969 (0.953–0.979)
$\text{ADC}_{0\text{Hz}}^{95\text{th}}$	0.862 (0.799–0.906)	0.987 (0.980–0.991)
$\text{ADC}_{50\text{Hz}}^{\text{mean}}$	0.967 (0.950–0.978)	0.992 (0.988–0.995)
$\text{ADC}_{50\text{Hz}}^{5\text{th}}$	0.908 (0.865–0.938)	0.962 (0.943–0.974)
$\text{ADC}_{50\text{Hz}}^{95\text{th}}$	0.889 (0.838–0.925)	0.990 (0.985–0.993)
cADC <sup>mean</sup>	0.974 (0.963–0.982)	0.995 (0.993–0.997)
cADC <sup>5th</sup>	0.825 (0.748–0.880)	0.982 (0.973–0.988)
cADC <sup>95th</sup>	0.981 (0.971–0.987)	0.992 (0.988–0.995)
rcADC <sup>mean</sup>	0.968 (0.953–0.979)	0.998 (0.997–0.998)
rcADC <sup>5th</sup>	0.868 (0.808–0.910)	0.983 (0.975–0.989)
rcADC <sup>95th</sup>	0.952 (0.929–0.968)	0.995 (0.992–0.997)

rcADC<sup>5th</sup> ( $p < 0.01$ ), and rcADC<sup>95th</sup> ( $p < 0.01$ ) values were significantly higher for brain metastases than for glioblastomas (Fig. 5d–i).

The  $\text{ADC}_{0\text{Hz}}^{\text{mean}}$ ,  $\text{ADC}_{0\text{Hz}}^{5\text{th}}$ ,  $\text{ADC}_{0\text{Hz}}^{95\text{th}}$ ,  $\text{ADC}_{50\text{Hz}}^{\text{mean}}$ ,  $\text{ADC}_{50\text{Hz}}^{5\text{th}}$ , and  $\text{ADC}_{50\text{Hz}}^{95\text{th}}$  values of the peritumoral regions for glioblastomas and brain metastases are shown in Fig. 6a–c. For both tumors, all three indices for  $\text{ADC}_{50\text{Hz}}$  were significantly higher than those for  $\text{ADC}_{0\text{Hz}}$  (all  $p < 0.01$ , respectively) (Fig. 6a–c). No significant difference in any of the three indices of  $\text{ADC}_{0\text{Hz}}$ ,  $\text{ADC}_{50\text{Hz}}$ , cADC, and rcADC was observed between brain metastases and glioblastomas (Fig. 6a–i).

#### Diagnostic performance in differentiating brain metastases from glioblastoma

The results of receiver operating characteristic (ROC) curve analyses are shown in Table 4. The ROC curve analysis showed significance for cADC<sup>mean</sup>, cADC<sup>95th</sup>, rcADC<sup>mean</sup>, rcADC<sup>5th</sup>, and rcADC<sup>95th</sup> (AUC = 0.877, 0.865, 0.819, 0.652, and 0.796; respectively;  $p < 0.01$ ,

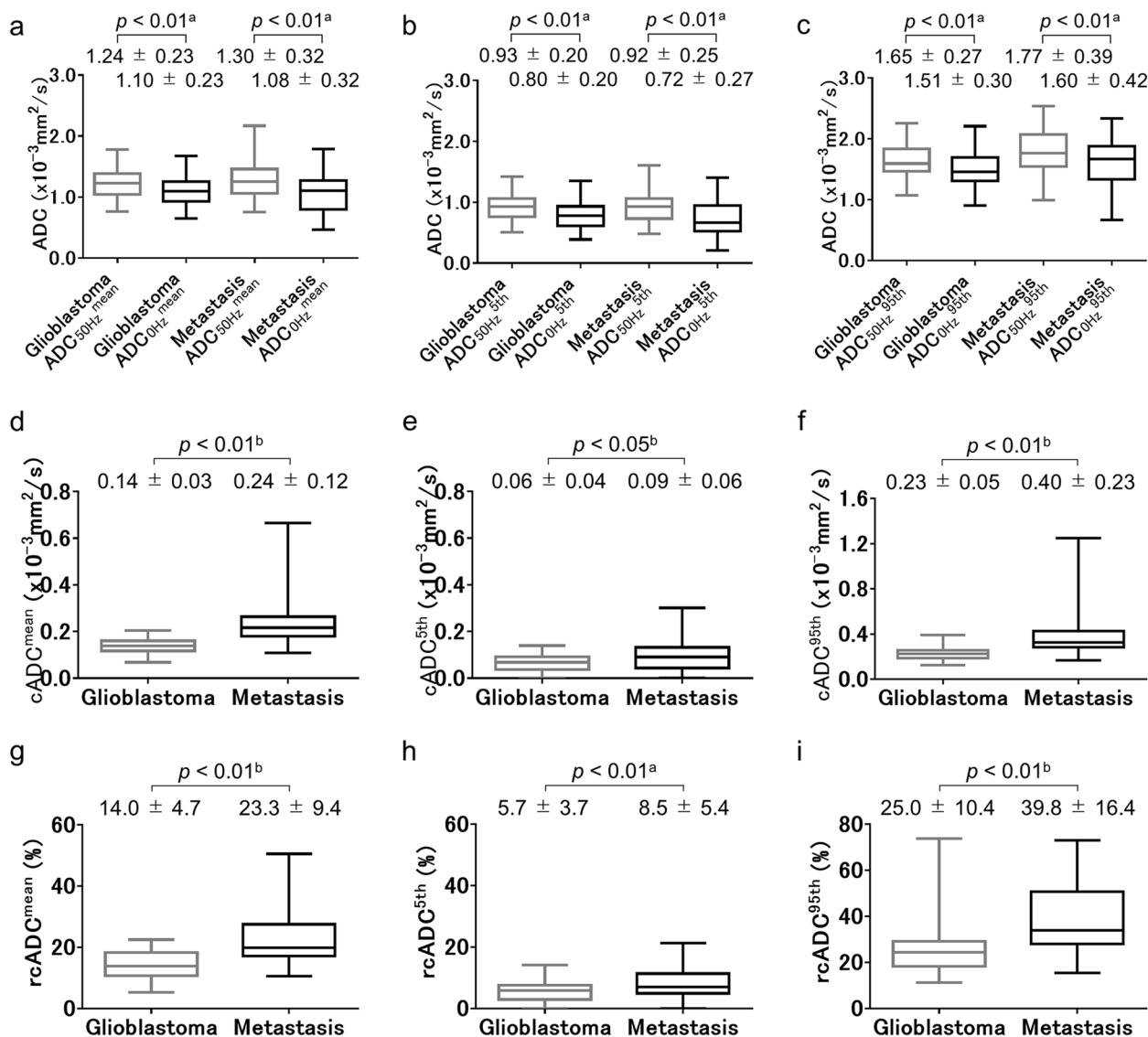


**Fig. 5** Box-whisker plots of ADC<sub>0Hz</sub><sup>mean</sup> and ADC<sub>50Hz</sub><sup>mean</sup> (a), ADC<sub>0Hz</sub><sup>5th</sup> and ADC<sub>50Hz</sub><sup>5th</sup> (b), and ADC<sub>0Hz</sub><sup>95th</sup> and ADC<sub>50Hz</sub><sup>95th</sup> (c) of enhancing regions for glioblastomas and brain metastases. For each tumor, each index for ADC<sub>50Hz</sub> was significantly higher than the corresponding index for ADC<sub>0Hz</sub> (each  $p < 0.01$ , respectively) (a–c). Box-whisker plots of cADC<sup>mean</sup> (d), cADC<sup>5th</sup> (e), and cADC<sup>95th</sup> (f) of enhancing regions for glioblastomas and brain metastases. Each index for cADC was significantly higher in brain metastases than in glioblastomas (each  $p < 0.01$ , respectively). Box-whisker plots of rcADC<sup>mean</sup> (g), rcADC<sup>5th</sup> (h), and rcADC<sup>95th</sup> (i) of enhancing regions for glioblastomas and brain metastases. Each index for rcADC was significantly higher in brain metastases than in glioblastomas (each  $p < 0.01$ , respectively). Statistical tests used: <sup>a</sup>paired-*t* test, <sup>b</sup>Mann–Whitney *U* test

$p < 0.01$ ,  $p < 0.01$ ,  $p = 0.02$ , and  $p < 0.01$ ; respectively), and their accuracy in diagnosing glioblastoma was 87.0%, 85.9%, 72.8%, 64.1%, and 79.3%; respectively. The most effective indices for the ADC<sub>0Hz</sub><sup>5th</sup>, ADC<sub>50Hz</sub><sup>95th</sup>, cADC<sup>mean</sup>, and rcADC<sup>mean</sup> were ADC<sub>0Hz</sub><sup>5th</sup>, ADC<sub>50Hz</sub><sup>95th</sup>, cADC<sup>mean</sup>, and rcADC<sup>mean</sup>, respectively. As shown in Table 5, pairwise comparisons of the AUC of ROC curves among those most effective indices revealed that the AUC of the cADC<sup>mean</sup> was significantly greater than those of ADC<sub>0Hz</sub><sup>5th</sup> ( $p < 0.001$ ) and ADC<sub>50Hz</sub><sup>95th</sup> ( $p = 0.004$ ) and

that the AUC of the rcADC<sup>mean</sup> was significantly greater than that of ADC<sub>0Hz</sub><sup>5th</sup> ( $p < 0.001$ ). No other comparisons of the AUCs revealed significant differences. The ROC curves for the ADC<sub>0Hz</sub><sup>5th</sup>, ADC<sub>50Hz</sub><sup>95th</sup>, cADC<sup>mean</sup>, and rcADC<sup>mean</sup> are shown in Fig. 7.

## Discussion

This study revealed no significant difference between brain metastases and glioblastomas in ADCs measured using short (7.1 ms) and long (44.5 ms) effective



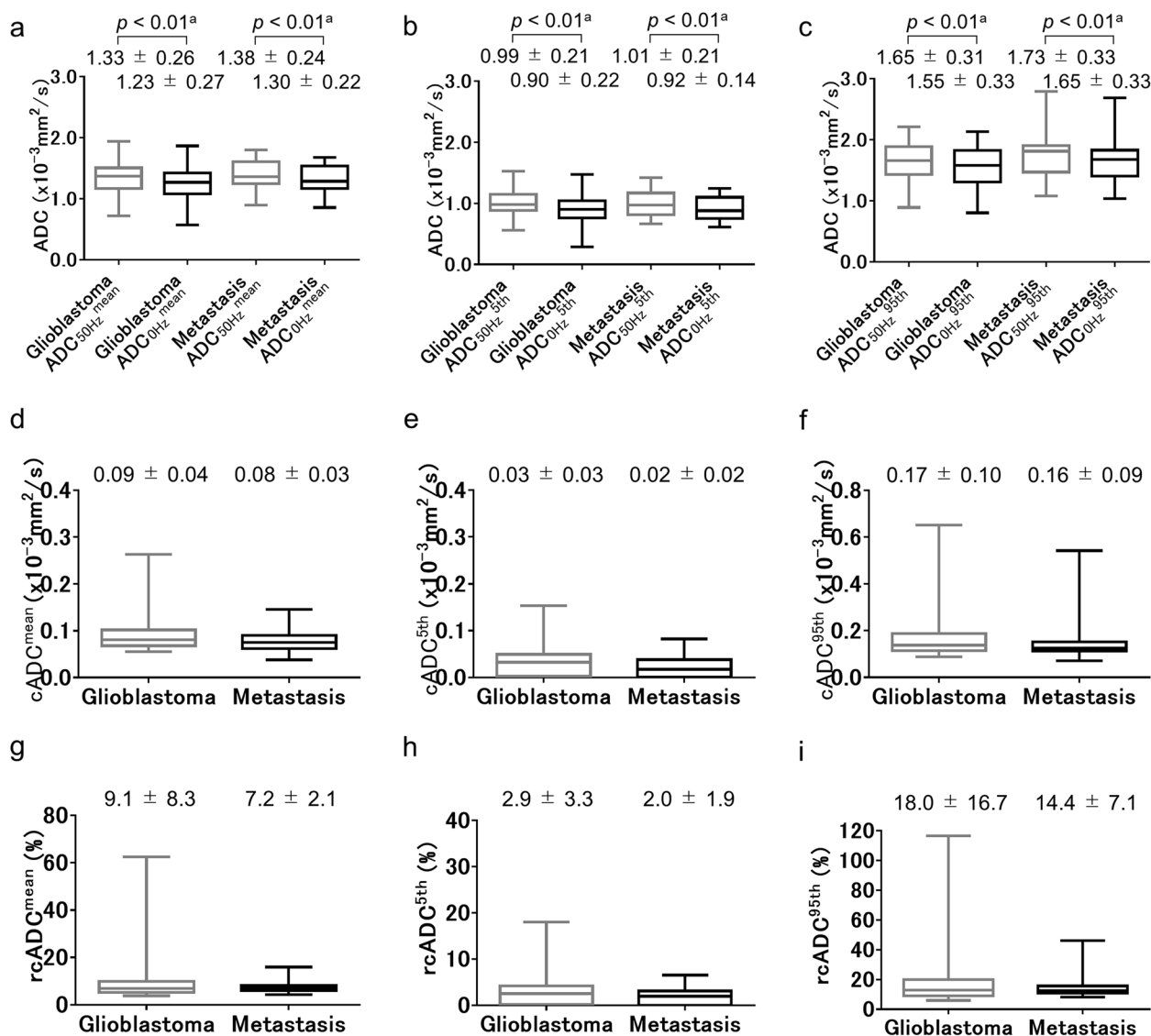


**Fig. 6** Box-whisker plots of ADC<sub>mean</sub> and ADC<sub>50Hz</sub> (a), ADC<sub>5th</sub> and ADC<sub>50Hz</sub> (b), and ADC<sub>95th</sub> and ADC<sub>50Hz</sub> (c) of peritumoral regions for glioblastomas and brain metastases. For each tumor, each index for ADC<sub>50Hz</sub> was significantly higher than the corresponding index for ADC<sub>0Hz</sub> (each  $p < 0.01$ , respectively) (a–c). Box-whisker plots of cADC<sub>mean</sub> (d), cADC<sub>5th</sub> (e), and cADC<sub>95th</sub> (f) of peritumoral regions for glioblastomas and brain metastases. Box-whisker plots of rcADC<sub>mean</sub> (g), rcADC<sub>5th</sub> (h), and rcADC<sub>95th</sub> (i) of peritumoral regions for glioblastomas and brain metastases. No significant difference in any of the three indices of ADC<sub>0Hz</sub>, ADC<sub>50Hz</sub>, cADC, and rcADC was observed between brain metastases and glioblastomas (Fig. 6a–i). Statistical tests used: <sub>a</sub>paired-*t* test, <sub>b</sub>Mann–Whitney *U* test

diffusion times, whereas both the change and relative change of ADC (cADC and rcADC, respectively) were significantly higher in brain metastases than in glioblastomas. Moreover, the ADC change, particularly the cADC<sub>mean</sub>, showed a good performance in differentiating brain metastases from glioblastomas, suggesting the clinical usefulness of time-dependent diffusion MRI for this purpose.

Time-dependent diffusion MRI using OGSE and PGSE DWI sequences has drawn increasing attention among the medical community of oncological

imaging. Previously, Iima et al. investigated the use of time-dependent diffusion MRI in distinguishing malignant head and neck tumors from benign ones, involving 56 patients [22]. They found that the relative change in ADC between short (4.3 ms) and long (82.6 ms) effective diffusion times was significantly higher in malignant head and neck tumors than benign ones. Maekawa et al. used two effective diffusion times (6.5 ms and 32.5 ms) and examined 21 brain tumors using time-dependent diffusion MRI and showed that both the ADC change and the relative ADC change were significantly higher for

**Table 4** The AUC, optimal threshold, sensitivity, specificity, and accuracy for  $ADC_{0Hz}^{mean}$ ,  $ADC_{0Hz}^{5th}$ ,  $ADC_{0Hz}^{95th}$ ,  $ADC_{50Hz}^{mean}$ ,  $ADC_{50Hz}^{5th}$ ,  $ADC_{50Hz}^{95th}$ ,  $cADC^{mean}$ ,  $cADC^{5th}$ ,  $cADC^{95th}$ ,  $rcADC^{mean}$ ,  $rcADC^{5th}$ , and  $rcADC^{95th}$  of the enhancing and peritumoral regions to differentiate brain metastases from glioblastomas

Parameter	AUC (95% CI)	p Value	Threshold value	Sensitivity (%)	Specificity (%)	Accuracy (%)
<b>Enhancing region</b>						
$ADC_{0Hz}^{mean}$	0.527 (0.420–0.632)	0.71	$0.800 (\times 10^{-3} \text{ mm}^2/\text{s})$	80.8	25.9	71.7
$ADC_{0Hz}^{5th}$	0.595 (0.487–0.696)	0.19	$0.683 (\times 10^{-3} \text{ mm}^2/\text{s})$	70.8	55.6	66.3
$ADC_{0Hz}^{95th}$	0.592 (0.485–0.694)	0.20	$1.659 (\times 10^{-3} \text{ mm}^2/\text{s})$	73.8	51.9	67.4
$ADC_{50Hz}^{mean}$	0.544 (0.437–0.649)	0.53	$1.350 (\times 10^{-3} \text{ mm}^2/\text{s})$	72.3	44.4	64.1
$ADC_{50Hz}^{5th}$	0.526 (0.419–0.631)	0.71	$0.664 (\times 10^{-3} \text{ mm}^2/\text{s})$	96.9	18.5	73.9
$ADC_{50Hz}^{95th}$	0.615 (0.508–0.714)	0.10	$1.704 (\times 10^{-3} \text{ mm}^2/\text{s})$	66.2	59.3	64.1
$cADC^{mean}$	0.877 (0.793–0.937)	< 0.01	$0.174 (\times 10^{-3} \text{ mm}^2/\text{s})$	89.2	81.5	87.0
$cADC^{5th}$	0.630 (0.523–0.729)	0.06	$0.081 (\times 10^{-3} \text{ mm}^2/\text{s})$	67.7	59.3	65.2
$cADC^{95th}$	0.865 (0.778–0.927)	< 0.01	$0.278 (\times 10^{-3} \text{ mm}^2/\text{s})$	87.7	81.5	85.9
$rcADC^{mean}$	0.819 (0.724–0.891)	< 0.01	16.8 (%)	69.2	81.5	72.8
$rcADC^{5th}$	0.652 (0.546–0.749)	0.02	6.65 (%)	63.1	66.7	64.1
$rcADC^{95th}$	0.796 (0.700–0.873)	< 0.01	30.6 (%)	84.6	66.7	79.3
<b>Peritumoral region</b>						
$ADC_{0Hz}^{mean}$	0.566 (0.459–0.669)	0.30	$1.156 (\times 10^{-3} \text{ mm}^2/\text{s})$	40.0	81.5	52.2
$ADC_{0Hz}^{5th}$	0.509 (0.402–0.615)	0.89	$0.669 (\times 10^{-3} \text{ mm}^2/\text{s})$	18.5	96.3	41.3
$ADC_{0Hz}^{95th}$	0.559 (0.452–0.662)	0.37	$1.615 (\times 10^{-3} \text{ mm}^2/\text{s})$	56.9	59.3	57.6
$ADC_{50Hz}^{mean}$	0.558 (0.450–0.661)	0.38	$1.242 (\times 10^{-3} \text{ mm}^2/\text{s})$	38.5	77.8	50.0
$ADC_{50Hz}^{5th}$	0.509 (0.403–0.615)	0.89	$1.267 (\times 10^{-3} \text{ mm}^2/\text{s})$	95.4	14.8	71.7
$ADC_{50Hz}^{95th}$	0.559 (0.452–0.662)	0.37	$1.691 (\times 10^{-3} \text{ mm}^2/\text{s})$	55.4	63.0	57.6
$cADC^{mean}$	0.598 (0.491–0.699)	0.14	$0.072 (\times 10^{-3} \text{ mm}^2/\text{s})$	69.2	48.1	63.0
$cADC^{5th}$	0.580 (0.473–0.682)	0.21	$0.038 (\times 10^{-3} \text{ mm}^2/\text{s})$	46.2	77.8	55.4
$cADC^{95th}$	0.569 (0.462–0.672)	0.30	$0.140 (\times 10^{-3} \text{ mm}^2/\text{s})$	49.2	70.4	55.4
$rcADC^{mean}$	0.507 (0.401–0.613)	0.91	9.0 (%)	70.8	3.7	51.1
$rcADC^{5th}$	0.568 (0.460–0.671)	0.29	2.6 (%)	47.7	70.4	54.3
$rcADC^{95th}$	0.506 (0.399–0.612)	0.92	8.7 (%)	24.6	96.3	45.7

**Table 5** Pairwise comparison of the AUCs among the  $ADC_{0Hz}^{5th}$ ,  $ADC_{50Hz}^{95th}$ ,  $cADC^{mean}$ , and  $rcADC^{mean}$  of the enhancing regions

Parameter	$rcADC^{mean}$	$cADC^{mean}$	$ADC_{50Hz}^{95th}$
$ADC_{0Hz}^{5th}$			
DBE	0.224	0.283	0.020
p	< 0.001	< 0.001	0.877
$ADC_{50Hz}^{95th}$			
DBE	0.204	0.263	
p	0.042	0.004	
$cADC^{mean}$			
DBE	0.059		
p	0.179		

DBE Difference between areas

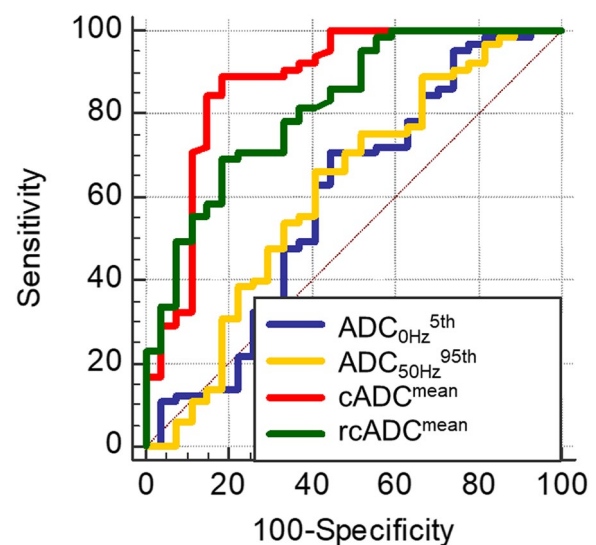


**Fig. 7** Receiver operating characteristic curves of the most effective indices for  $ADC_{0Hz}^{5th}$ ,  $ADC_{50Hz}^{95th}$ ,  $cADC^{mean}$ , and  $rcADC^{mean}$

high-grade tumors than for low-grade tumors [23]. Wu et al. used time-dependent MRI to examine the microstructures of 48 prostate cancers [30]. They reported that a higher histopathologic grade was significantly correlated with higher intracellular volume fraction and cellularity derived using a two-compartment diffusion model [31], and that cellularity achieved high performance in discriminating between clinically significant and insignificant prostate cancers. These studies demonstrated the clinical feasibility and relevance of time-dependent diffusion MRI. Nevertheless, none of these studies explicitly demonstrated the superiority of time-dependent diffusion MRI parameters over the conventional ADC. This is the first study to provide evidence that time-dependent diffusion MRI has additional clinical value as compared with conventional DWI.

Researchers have paid attention to the peritumoral regions in connection with the imaging differentiation of glioblastomas and brain metastases [32, 33]. Studies have investigated the use of peritumoral ADC for the differentiation of brain metastases from glioblastomas; however, its clinical value remains controversial. Lee et al. [11] reported that the minimum ADC in the peritumoral regions was useful in discriminating brain metastases from glioblastomas, whereas Tepe et al. [12] did not replicate this finding. This study revealed no significant difference in any of the peritumoral ADC indices between the two tumor types. To the best of our knowledge, time-dependent diffusion MRI has not been used to analyze peritumoral diffusion for the differentiation between brain metastases and glioblastomas. Our preliminary results suggest that ADC diffusion time dependence in the peritumoral region is not a sensitive marker for differentiating between brain metastases and glioblastomas.

Numerous studies have been published regarding MRI-based discrimination of brain metastases and glioblastomas, for which various promising structural and functional imaging parameters were reported, such as cerebral blood volume within the contrast-enhancing tumor and its surrounding areas with T2-prolongation [9] and amide proton transfer-related signal intensity in the enhancing tumor [34]. Our findings should be compared with those previous reports in future studies.

The underlying mechanism for the stronger ADC diffusion time dependence in brain metastases than in glioblastoma is unknown. In previous studies, stronger diffusion time dependence of ADC in malignant (or high-grade) tumors than in benign (or low-grade) tumors was attributed to more microstructures, which

restrict water molecular motion within the range of diffusion lengths determined by the selected short and long diffusion times in the OGSE and PGSE DWI sequences, respectively [22, 23]. Although this study lacks histopathological correlation, stronger ADC diffusion time dependence in brain metastases than in glioblastomas shown in this study appears to be consistent with the hypothesized higher intracellular volume fraction in metastatic tumors than in glioblastomas. Most brain metastases originate from epithelial tumors, such as cancers of the lung, breast, and colon. Epithelial tumors are characterized by cell–cell adhesion, which, in normal tissues, determines the polarity of cells and contributes to the maintenance of tissues [35]. In contrast, glioblastomas, as nonepithelial tumors, lack cell–cell adhesion, and are characterized by microvascular proliferation and necrosis [26]. To the best of our knowledge, no data regarding the histopathological comparison of intracellular volume fraction between glioblastomas and brain metastases have been published. A recent imaging study using Vascular, Extracellular, and Restricted Diffusion for Cytometry in Tumors (VERDICT) MRI compared two metastatic brain tumors (melanomas) and five glioblastomas, and showed distinctly higher intracellular volume fraction and lower extracellular volume fraction in metastases [36]. Despite the small sample size and inclusion of only one histological type of metastasis, their results from VERDICT MRI support our speculation.

An alternative explanation for the stronger ADC diffusion time dependence in brain metastases is the difference in cell size between the two tumor types. At a given set of diffusion times (and hence diffusion length), the diffusion time dependence of ADC could vary with cell size [37]. It is possible that the cell size of brain metastases was closer to the “sweet spot” range for our diffusion time settings than that of glioblastomas. Further studies are needed to elucidate the pathological basis that accounts for our findings.

#### Limitations of the study

This study has several limitations. First, the patient population was small; therefore, our suggested threshold ADC values, value of ADC difference, or relative ADC change might not be representative of those of a larger population. Second, only two diffusion times (one each for OGSE and PGSE sequences) and a fixed set of b-values (0 and 1,500 s/mm<sup>2</sup>) were investigated. Third, current clinical MRI systems limit OGSE to a relatively low frequency (50 Hz); therefore, the effective diffusion time was limited to 7.1 ms. Finally, we evaluated multiple types of brain

metastases with a small number of each type; therefore, comparing our results using histopathology was difficult. If each tumor type is evaluated, estimating the microstructure in more detail may be possible by comparing the findings using specific histopathological features.

## Conclusions

The time-dependent diffusion MRI parameters, particularly the mean of changes in the ADC value between short and long diffusion times obtained using the OGSE and PGSE methods in the enhancing regions, may be useful in differentiating brain metastases from glioblastomas.

## Abbreviations

MRI	Magnetic resonance imaging
DWI	Diffusion-weighted imaging
ADC	Apparent diffusion coefficient
PGSE	Pulsed gradient spin-echo
OGSE	Oscillating gradient spin-echo
$\Delta_{\text{eff}}$	Effective diffusion time
$\delta$	Diffusion gradient pulse duration
$\Delta$	Diffusion gradient separation
TR	Repetition time
TE	Echo time
FOV	Field of view
FLAIR	Fluid-attenuated inversion recovery
ROI	Region of interest
cADC	Apparent diffusion coefficient change
rcADC	Relative apparent diffusion coefficient change
ICC	Intraclass correlation coefficient
AUC	Area under the receiver operating characteristic curve
ROC	Receiver operating characteristic

## Acknowledgements

The authors wish to thank the staffs of Kagoshima University Hospital for their support.

## Authors' contributions

Kiyohisa Kamimura: Conceptualization, Data curation, Formal analysis, Investigation, Methodology, Project administration, Writing – original draft; Yoshiaki Kamimura: Data curation; Tsubasa Nakano: Data curation; Tomohito Hasegawa: Data curation; Masanori Nakajo: Data curation; Chihiro Yamada: Data curation; Kentaro Akune: Data curation; Fumitaka Ejima: Data curation; Koji Takumi: Data curation; Masatoyo Nakajo: Data curation; Hiroyuki Uchida: Data curation; Kazuhiro Tabata: Data curation; Takashi Iwanaga: Data curation; Hiroshi Imai: Software, Visualization; Thorsten Feiweier: Software, Visualization; Takashi Yoshiura: Conceptualization, Funding acquisition, Methodology, Project administration, Writing – review & editing. The authors read and approved the final manuscript.

## Funding

Not applicable.

## Availability of data and materials

The datasets of current study are available from the corresponding author on reasonable request.

## Declarations

### Ethics approval and consent to participate

This retrospective study was approved by our Institutional Ethics Review Board (Ethics Committee on Epidemiological Studies Kagoshima University Graduate School of Medical and Dental Sciences; no. 220126), and the requirement for informed consent of patients was waived.

## Consent for publication

Not applicable.

## Competing interests

Authors have no conflict of interest.

## Author details

<sup>1</sup>Department of Advanced Radiological Imaging, Kagoshima University Graduate School of Medical and Dental Sciences, 8-35-1 Sakuragaoka, Kagoshima 890-8544, Japan. <sup>2</sup>Department of Radiology, Kagoshima University Graduate School of Medical and Dental Sciences, 8-35-1 Sakuragaoka, Kagoshima 890-8544, Japan. <sup>3</sup>Department of Neurosurgery, Kagoshima University Graduate School of Medical and Dental Sciences, 8-35-1 Sakuragaoka, Kagoshima 890-8544, Japan. <sup>4</sup>Department of Pathology, Kagoshima University Graduate School of Medical and Dental Sciences, 8-35-1 Sakuragaoka, Kagoshima 890-8544, Japan. <sup>5</sup>Department of Radiological Technology, Kagoshima University Hospital, 8-35-1 Sakuragaoka, Kagoshima 890-8544, Japan. <sup>6</sup>Siemens Healthcare K.K., Gate City Osaki West Tower, 1-11-1 Osaki, Shinagawa-Ku, Tokyo 141-8644, Japan. <sup>7</sup>Siemens Healthcare GmbH, Henkstrasse 127, 91052 Erlangen, Germany.

Received: 14 May 2023 Accepted: 24 July 2023

Published: 8 August 2023

## References

- Giese A, Westphal M. Treatment of malignant glioma: a problem beyond the margins of resection. *J Cancer Res Clin Oncol*. 2001;127:217–25. <https://doi.org/10.1007/s004320000188>.
- Oh J, Cha S, Aiken AH, Han ET, Crane JC, Stainsby JA, et al. Quantitative apparent diffusion coefficients and T2 relaxation times in characterizing contrast enhancing brain tumors and regions of peritumoral edema. *J Magn Reson Imaging*. 2005;21:701–8. <https://doi.org/10.1002/jmri.20335>.
- Chen L, Liu M, Bao J, Xia Y, Zhang J, Zhang L, et al. The correlation between apparent diffusion coefficient and tumor cellularity in patients: a meta-analysis. *PLOS ONE*. 2013;8:e79008. <https://doi.org/10.1371/journal.pone.0079008>.
- Eidel O, Neumann JO, Burth S, Kieslich PJ, Jungk C, Sahm F, et al. Automatic analysis of cellularity in glioblastoma and correlation with ADC Using trajectory analysis and automatic nuclei counting. *PLoS One*. 2016;11:e0160250. <https://doi.org/10.1371/journal.pone.0160250>.
- Surov A, Meyer HJ, Wienke A. Correlation between apparent diffusion coefficient (ADC) and cellularity is different in several tumors: a meta-analysis. *Oncotarget*. 2017;8:59492–9. <https://doi.org/10.18632/oncotarget.17752>.
- Surov A, Ginat DT, Sanverdi E, Lim CCT, Hakyemez B, Yogi A, et al. Use of diffusion weighted imaging in differentiating between malignant and benign meningiomas. A multicenter analysis. *World Neurosurg*. 2016;88:598–602. <https://doi.org/10.1016/j.wneu.2015.10.049>.
- Kono K, Inoue Y, Nakayama K, Shakudo M, Morino M, Ohata K, et al. The role of diffusion-weighted imaging in patients with brain tumors. *AJNR Am J Neuroradiol*. 2001;22:1081–8.
- Eisenhut F, Schmidt MA, Putz F, Lettmaier S, Fröhlich K, Arinrad S, et al. Classification of primary cerebral lymphoma and glioblastoma featuring dynamic susceptibility contrast and apparent diffusion coefficient. *Brain Sci*. 2020;10:886. <https://doi.org/10.3390/brainsci10110886>.
- Cindil E, Sendur HN, Cerit MN, Dag N, Erdogan N, Celebi FE, et al. Validation of combined use of DWI and percentage signal recovery-optimized protocol of DSC-MRI in differentiation of high-grade glioma, metastasis, and lymphoma. *Neuroradiology*. 2021;63:331–42. <https://doi.org/10.1007/s00234-020-02522-9>.
- Zhang G, Chen X, Zhang S, Ruan X, Gao C, Liu Z, et al. Discrimination between solitary brain metastasis and glioblastoma multiforme by using ADC-based texture analysis: a comparison of two different ROI placements. *Acad Radiol*. 2019;26:1466–72. <https://doi.org/10.1016/j.jacr.2019.01.010>.
- Lee EJ, terBrugge K, Mikulis D, Choi DS, Bae JM, Lee SK, et al. Diagnostic value of peritumoral minimum apparent diffusion coefficient for differentiation of glioblastoma multiforme from solitary metastatic lesions. *AJR Am J Roentgenol*. 2011;196:71–6. <https://doi.org/10.2214/AJR.10.4752>.



12. Tepe M, Saylisoy S, Toprak U, Inan I. The potential role of peritumoral apparent diffusion coefficient evaluation in differentiating glioblastoma and solitary metastatic lesions of the brain. *Curr Med Imaging*. 2021;17:1200–8. <https://doi.org/10.2174/1573405617666210316120314>.
13. Maekawa T, Hori M, Murata K, Feiweier T, Fukunaga I, Andica C, et al. Changes in the ADC of diffusion-weighted MRI with the oscillating gradient spin-echo (OGSE) sequence due to differences in substrate viscosities. *Jpn J Radiol*. 2018;36:415–20. <https://doi.org/10.1007/s11604-018-0737-0>.
14. Baron CA, Beaulieu C. Oscillating gradient spin-echo (OGSE) diffusion tensor imaging of the human brain. *Magn Reson Med*. 2014;72:726–36. <https://doi.org/10.1002/mrm.24987>.
15. Portnoy S, Fichtner ND, Dziegielewska C, Stanisz MP, Stanisz GJ. In vitro detection of apoptosis using oscillating and pulsed gradient diffusion magnetic resonance imaging. *NMR Biomed*. 2014;27:371–80. <https://doi.org/10.1002/nbm.3070>.
16. Wu D, Martin LJ, Northington FJ, Zhang J. Oscillating gradient diffusion MRI reveals unique microstructural information in normal and hypoxia-ischemia injured mouse brains. *Magn Reson Med*. 2014;72:1366–74. <https://doi.org/10.1002/mrm.25441>.
17. Pyatigorskaya N, Le Bihan D, Reynaud O, Ciobanu L. Relationship between the diffusion time and the diffusion MRI signal observed at 17.2 Tesla in the healthy rat brain cortex. *Magn Reson Med*. 2014;72:492–500. <https://doi.org/10.1002/mrm.24921>.
18. Stejskal EO, Tanner JE. Spin diffusion measurements: spin echoes in the presence of a time-dependent field gradient. *J Chem Phys*. 1965;42:288–92. <https://doi.org/10.1063/1.1695690>.
19. Stejskal EO. Use of spin echoes in a pulsed magnetic-field gradient to study anisotropic, restricted diffusion and flow. *J Chem Phys*. 1965;43:3597–603. <https://doi.org/10.1063/1.1696526>.
20. Van AT, Holdsworth SJ, Bammer R. In vivo investigation of restricted diffusion in the human brain with optimized oscillating diffusion gradient encoding. *Magn Reson Med*. 2014;71:83–94. <https://doi.org/10.1002/mrm.24632>.
21. Andica C, Hori M, Kamiya K, Koshino S, Hagiwara A, Kamagata K, et al. Spatial restriction within intracranial epidermoid cysts observed using short diffusion-time diffusion-weighted imaging. *Magn Reson Med Sci*. 2018;17:269–72. <https://doi.org/10.2463/mrms.cr.2017-0111>.
22. Iima M, Yamamoto A, Kataoka M, Yamada Y, Omori K, Feiweier T, et al. Time-dependent diffusion MRI to distinguish malignant from benign head and neck tumors. *J Magn Reson Imaging*. 2019;50:88–95. <https://doi.org/10.1002/jmri.26578>.
23. Maekawa T, Hori M, Murata K, Feiweier T, Kamiya K, Andica C, et al. Differentiation of high-grade and low-grade intra-axial brain tumors by time-dependent diffusion MRI. *Magn Reson Imaging*. 2020;72:34–41. <https://doi.org/10.1016/j.mri.2020.06.018>.
24. Reynaud O, Winters KV, Hoang DM, Wadghiri YZ, Novikov DS, Kim SG. Pulsed and oscillating gradient MRI for assessment of cell size and extracellular space (POMACE) in mouse gliomas. *NMR Biomed*. 2016;29:1350–63. <https://doi.org/10.1002/nbm.3577>.
25. Higa N, Akahane T, Yokoyama S, Yonezawa H, Uchida H, Takajo T, et al. A tailored next-generation sequencing panel identified distinct subtypes of wildtype IDH and TERT promoter glioblastomas. *Cancer Sci*. 2020;111:3902–11. <https://doi.org/10.1111/cas.14597>.
26. Louis DN, Perry A, Brat DJ, Pfister SM, Ellison DW, Reifenberger G, et al. WHO classification of tumours of the central nervous system. 5th ed. Lyon: IARC; 2021. p. 15–187, 349–69.
27. Does MD, Parsons EC, Gore JC. Oscillating gradient measurements of water diffusion in normal and globally ischemic rat brain. *Magn Reson Med*. 2003;49:206–15. <https://doi.org/10.1002/mrm.10385>.
28. Chung WJ, Kim HS, Kim N, Choi CG, Kim SJ. Recurrent glioblastoma: optimum area under the curve method derived from dynamic contrast-enhanced T1-weighted perfusion MR imaging. *Radiology*. 2013;269:561–8. <https://doi.org/10.1148/radiol.13130016>.
29. Shrout PE, Fleiss JL. Intraclass correlations: uses in assessing rater reliability. *Psychol Bull*. 1979;86:420–8. <https://doi.org/10.1037//0033-2909.86.2.420>.
30. Wu D, Jiang K, Li H, Zhang Z, Ba R, Zhang Y, et al. Time-dependent diffusion MRI for quantitative microstructural mapping of prostate cancer. *Radiology*. 2022;303:578–87. <https://doi.org/10.1148/radiol.211180>.
31. Jiang X, Li H, Xie J, McKinley ET, Zhao P, Gore JC, et al. In vivo imaging of cancer cell size and cellularity using temporal diffusion spectroscopy. *Magn Reson Med*. 2017;78:156–64. <https://doi.org/10.1002/mrm.26356>.
32. Martín-Noguerol T, Mohan S, Santos-Armentia E, Cabrera-Zubizarreta A, Luna A. Advanced MRI assessment of non-enhancing peritumoral signal abnormality in brain lesions. *Eur J Radiol*. 2021;143:109900. <https://doi.org/10.1016/j.ejrad.2021.109900>.
33. Scola E, Del Vecchio G, Busto G, Bianchi A, Desideri I, Gadda D, et al. Conventional and advanced magnetic resonance imaging assessment of non-enhancing peritumoral area in brain tumor. *Cancers*. 2023;15:2992. <https://doi.org/10.3390/cancers15112992>.
34. Kamimura K, Nakajo M, Yoneyama T, Fukukura Y, Hirano H, Goto Y, et al. Histogram analysis of amide proton transfer-weighted imaging: comparison of glioblastoma and solitary brain metastasis in enhancing tumors and peritumoral regions. *Eur Radiol*. 2019;29:4133–40. <https://doi.org/10.1007/s00330-018-5832-1>.
35. Hirohashi S, Kanai Y. Cell adhesion system and human cancer morphogenesis. *Cancer Sci*. 2003;94:575–81. <https://doi.org/10.1111/j.1349-7006.2003.tb01485.x>.
36. Figini M, Castellano A, Bailo M, Callea M, Cadioli M, Bouyagoub S, et al. Comprehensive brain tumour characterisation with VERDICT-MRI: evaluation of cellular and vascular measures validated by histology. *Cancers*. 2023;15:2490. <https://doi.org/10.3390/cancers15092490>.
37. Jiang X, Li H, Xie J, Zhao P, Gore JC, Xu J. Quantification of cell size using temporal diffusion spectroscopy. *Magn Reson Med*. 2016;75:1076–85. <https://doi.org/10.1002/mrm.25684>.

## Publisher's Note

Springer Nature remains neutral with regard to jurisdictional claims in published maps and institutional affiliations.